CHAPTER 30

An Overview of Numerical Weather Prediction

Bruce B. Ross

30.1. A Brief History of Operational Numerical Weather Prediction in the United States

Starting with the first barotropic model experiments of Charney and Von Neumann in 1950 (Charney *et al.*, 1950), numerical models of the atmosphere have developed into the primary means by which forecasters are able to predict synoptic-scale weather beyond 6 h. The success of the early numerical experiments of Charney led, in 1954, to the formation of the Joint Numerical Weather Forecasting Unit in Washington, D.C., with the purpose of developing operational versions of these research models. The first operational numerical model, a geostrophic barotropic model of the Northern Hemisphere, was introduced as an objective forecasting tool for National Weather Service (NWS) forecasters in 1958. This model (Cressman, 1958) contained much of the same physics as had been used by Charney and his associates in 1950. However, because of improvements in computer speed and capacity,* enhanced communication capabilities, and refinements in the original barotropic model, two-dimensional barotropic forecasts out to several days could be provided in a timely fashion to field forecasters. Significant improvements in 36 h, 500 mb predictions over subjective forecasts resulted from the introduction of this first objective forecast.

Figure 30.1 summarizes the increase in 36 h forecasting skill between 1955 and 1981 as operational forecasting models were improved. The initial improvements that the barotropic model made in the 500 mb forecasts were followed by improvements in the surface forecasts as well when a three-level baroclinic filtered-equation (geostrophic) model (an outgrowth of Charney's [1954] n level research model) became operational in 1962. During this period, an increasing number of rawinsonde stations, located in North America, on some 20 ships, and in foreign countries, were providing upper-air

* In the 1950 experiments, the ENIAC computer had required 36 h to complete a 24 h forecast (Platzman, 1979).

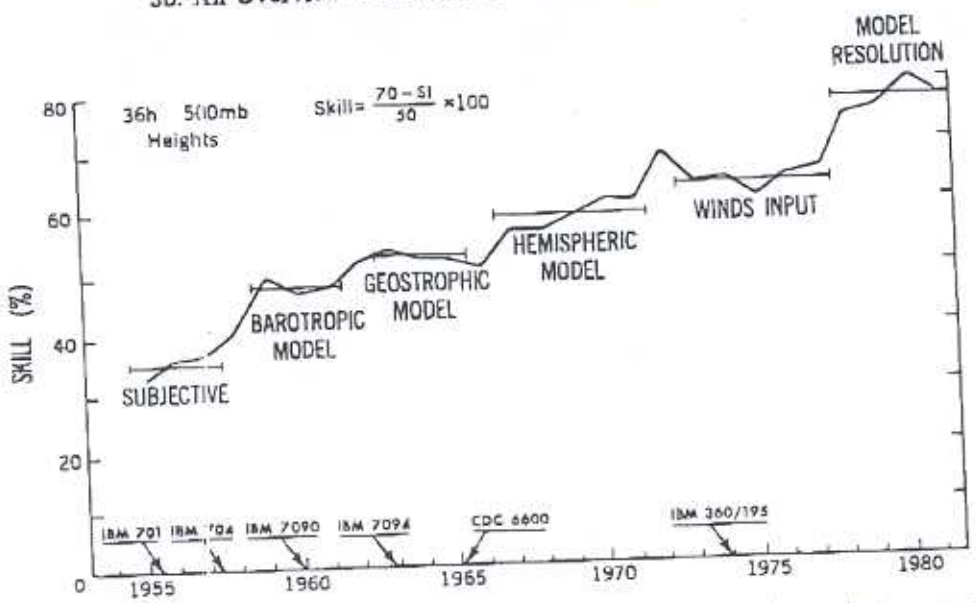

Figure 50.1. The accuracy of short-range weather prediction from the time prior to numerical weather prediction to 1981. The curve indicates the skill, averaged annually, of subjective and objective forecasts in predicting 500 mb heights at 36 h. The skill parameter is related, by the formula shown, to the so-called S_1 score (Teweles and Wobus, 1954) which is a measure of the normalized error in horizontal pressure gradients. Important changes in operational models and installation dates for different computer systems at NMC are indicated. (Data from the NMC; figure courtesy of William Bonner and Kiku Miyakoda.)

data twice daily for use as initial conditions for the hemispheric model forecasts. The six-level, hemispheric, primitive equation (PE) model (Shuman and Hovermale, 1968), which became operational in 1966, likewise benefited from the earlier research of others as well as the extensive development work at the National Meteorological Center (NMC), which was formed in 1961.

The Limited-area Fine-Mesh (LFM) model, introduced in 1971, was a limited-domain version of this hemispheric PE model. The LFM model provided increased horizontal resolution over North America, the region of primary importance for short-range forecasts of synoptic weather systems. This model represented the first operational version of a regional forecasting system and contained some features of what we would now call mesoscale numerical models. As an outgrowth of the limited-area model, the higher resolution Movable Fine-Mesh (MFM) model was introduced in 1975 for use in an "on-call" basis to forecast hurricane movement as well as intense precipitation patterns in severe weather conditions.

About 1972, observed winds were incorporated directly into models' initial conditions: prior to this, initial wind fields were derived from observed geopotential heights by means of a balance equation. A data assimilation system was made operational in 1974 to improve the ongoing analysis of observational data and their incorporation into the global PE model. In 1978, the horizontal grid size of the hemispheric model was halved to match that of

the LFM model. Finally, in 1980, the grid-point hemispheric PE model was replaced by a 12 level global spectral model that predicts large-scale features for periods of 5–10 days.

30.2. Comparison of Mesoscale and Global-Scale Numerical Models

The evolution of operational numerical weather prediction (NWP) from larger to smaller grid scales partially reflects the increased computer power that has allowed global models to resolve more details of atmospheric flow fields. However, more specialized limited-area models, such as the LFM and MFM operational models, have also permitted the simulation and forecasting of subsynoptic and mesoscale weather phenomena.

In fact, just as early operational numerical models were preceded by experimental research models, so also the increased emphasis of operational NWP on smaller scales has been preceded by an increased research interest in mesoscale modeling. The last ten years have seen considerable advancement in the simulation of many mesoscale phenomena in a research environment. The diversity of mesoscale modeling efforts has reflected the great diversity of mesoscale phenomena. Hence, the different types of mesoscale models have traditionally been categorized as follows. (Relevant review papers are listed after each; also see Haltiner and Williams, 1980, for a review of numerical weather prediction, and Pielke, 1984, for a general review of mesoscale modeling.)

- Regional-scale phenomena (Kreitzberg, 1979; Anthes, 1983; UCAR, 1983).
- Hurricanes (Anthes, 1982; Ooyama, 1982).
- Orographically forced flows (Pielke, 1981; UCAR, 1983).
- Convective clouds (Cotton, 1975; Schlesinger, 1982; Farley and Orville, 1982; Clark, 1982).

The classifications are somewhat arbitrary. For example, regional-scale simulations will certainly contain terrain effects. Likewise, hurricane models, which use several different grid sizes within the model domain, could conceivably resolve certain aspects of convective cloud phenomena if high-resolution regions of the model had sufficiently small grid size. This section addresses the primary features that distinguish mesoscale models from their more classical global-scale counterparts.

30.2.1. Phenomena To Be Modeled

The phenomena that are to be simulated determine the attributes required of the numerical model. Hence, if one wishes to forecast the evolution of baroclinic waves (with wavelength >2000 km) for a period of several days to a week, a global-scale model such as the NMC spectral PE model would be required, capable of resolving the smallest important baroclinic waves and with representation of physical processes such as radiation, cumulus convection, and boundary layer effects in a manner appropriate to the large space and time scales of the waves.

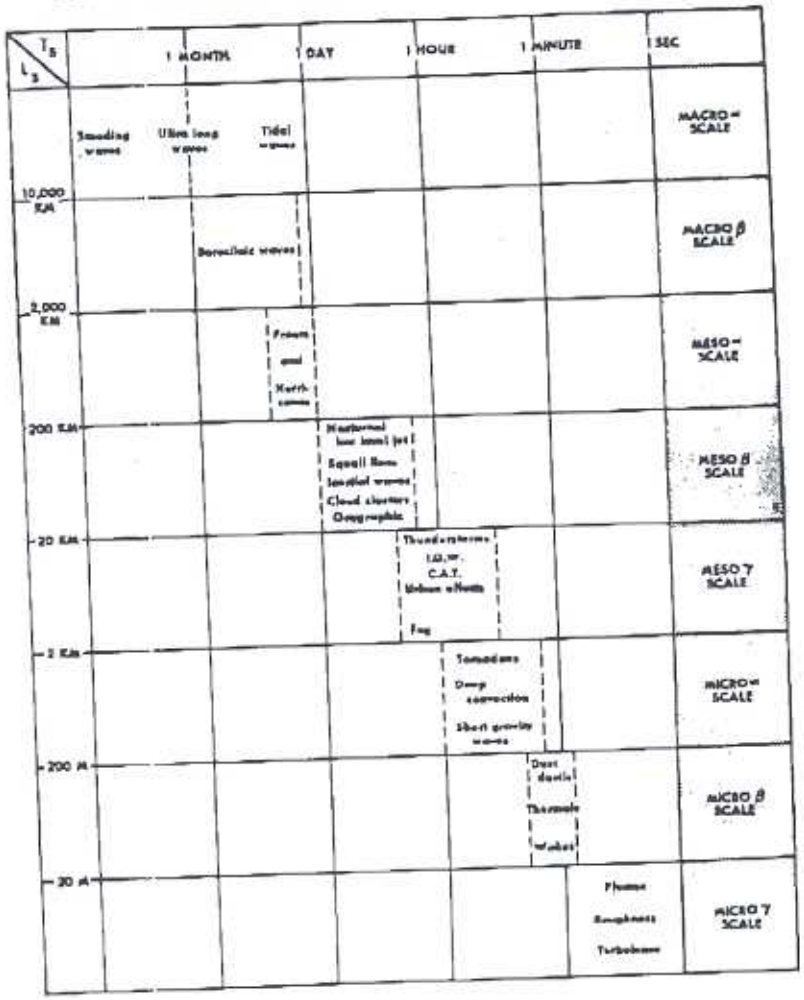

Figure 30.2. Scale definition proposed by Orlanski, with examples of atmospheric processes and their corresponding time and horizontal space scales. Representative physical time scales are given at the top. (After Orlanski, 1975; see also Fig. 2.12, this volume.)

When mesoscale phenomena are to be modeled, however, the spatial and temporal scales to be resolved may be smaller by an order of magnitude or more. Figure 30.2 shows the differences in time and space scales between macroscale and mesoscale weather systems and processes. A numerical model that is to represent these phenomena must be correct not only in its spatial resolution and domain design, but also in the types of physical processes that are included and the way in which they are represented (or parameterized).

30.2.2. Grid Resolution and Domain Size

As in models representing baroclinic waves, the grid size (i.e., the distance between adjacent points in the gridded domain) of a mesoscale model

should ideally be determined by the smallest scale associated with the phenomenon of interest. It is desirable that the smallest wave-like features be 4–6 times the grid size in order to reduce numerical (truncation) errors in wave propagation and advection to acceptable levels (see Pielke, 1981). (Such criteria may be difficult to follow when convection is present, since the most unstable scales for convection decrease to zero in a hydrostatic model [Orlanski, 1981].) For example, if one wishes to model the meso-α-scale structure of a hurricane (without trying to resolve the structure of the hurricane eye) with a scale of several hundred kilometers, then a horizontal grid size of roughly 50 km is needed. The integration of a global-scale model with 50 km horizontal resolution and a vertical resolution of 6–10 levels would be a major undertaking even for present-day supercomputers. The obvious solution is to use a limited-area domain, and communicate information about conditions outside the domain through lateral boundary conditions. (Nesting techniques are discussed in Sec. 30.3.)

30.2.3. Parameterization of Physical Processes

Many of the physical processes that are treated in synoptic-scale numerical models should also be included in their meso-α (regional)-scale and meso-β-scale counterparts. However, because of the reduced spatial and temporal scales of the mesoscale model, the processes will have increased importance in the simulation and may require a more detailed treatment than in corresponding large-scale versions. (See Anthes [1983] for a review of different treatments of physical processes in regional-scale models.)

Figure 30.2 helps to explain the increased importance of subgrid-scale processes in mesoscale models. Resolvable scales in synoptic and global systems are confined to the macro-α and macro-β length scales; the predominant subgrid effects, cumulus convection and turbulence, occur on scales of meso-γ and smaller. Hence, these parameterized effects are energetically quite separate in spatial scales from the important processes treated by the synoptic-scale model and can probably be treated effectively in a statistical sense. In a mesoscale model, on the other hand, resolved scales, such as the meso-α and meso-β, border on those categories that must still be parameterized. Hence these subgrid phenomena must be represented in a more detailed manner by the mesoscale model, because they are more energetically significant to the model representation.

Cumulus parameterization provides a good example of the need for different formulations between synoptic-scale and mesoscale models. Cumulus convection may be treated in synoptic-scale models as large cumulus cloud ensembles within a grid box (Arakawa and Schubert, 1974), since the grid spacing is hundreds of kilometers. In a mesoscale model with a grid size of 50 km, however, this statistical representation of convection is not so useful (since cumulus cloud elements each will have a horizontal scale of a kilometer or more and a spatial separation of the same order). A satisfactory parameterization of cumulus convection has yet to be demonstrated for mesoscale models, although a number of different methods have been proposed. In fact, ultimately the best approach to cumulus convection in a mesoscale

model may not be to parameterize it, but rather to let the model attempt to resolve it if sufficiently high resolution is feasible (Rosenthal, 1978; Ross and Orlanski, 1978).

As a second example, in a synoptic-scale model used only for short-range forecasts, details of the vertical dynamic and thermodynamic structure of the planetary boundary layer may be of only secondary importance. As shown by Carlson *et al.* (1983), however, such details may be quite important for the mesoscale simulation of convective outbreaks. Therefore, although the representation of boundary layer and surface processes can be fairly simple for a short-range synoptic forecasting model (surface effects become important in synoptic models as the temporal forecast range is extended), a fairly elaborate representation of surface and boundary layer physics may be necessary for mesoscale forecasting of the environment of convective events.

30.2.4. Data Sources

For the simulation of synoptic-scale baroclinic waves, a satisfactory representation of the initial atmospheric state can be derived from the operational rawinsonde network, supplemented by aircraft and satellite data over the data-sparse ocean regions. However, the horizontal resolution of such a data set is sufficient only to resolve coarse mesoscale features. Hence, if it is necessary to initialize a mesoscale forecast with detailed mesoscale features (in analogy with the global model's resolution of baroclinic waves), high resolution observations are needed. For example, detailed observations from aircraft are potentially important for defining the initial storm structure in operational hurricane track forecasts.

Although such mesoscale observations are highly desirable and can be obtained from ground- and satellite-based remote sensing systems, their extensive use in operational forecasting systems is unlikely in the near future. Until such mesoscale data sources become available, idealized initial conditions must be used, as they are in many research models and in the hurricane track forecasting models, or else the model must be allowed to generate its own mesoscale features from larger-scale initial conditions, as has been demonstrated in a number of mesoscale simulations (e.g., Anthes *et al.*, 1982; Orlanski and Polinsky, 1984).

30.2.5. Initialization Procedures

The initialization of mesoscale models is discussed in Ch. 8 and Ch. 25 of this volume. Several points are made here, however, to contrast the initialization of mesoscale and of large-scale models: (1) Whereas initialization procedures that assume geostrophic balance conditions may be quite suitable for modeling synoptic weather conditions, such balance assumptions become progressively less appropriate as the horizontal scale L of the phenomenon decreases. The Rossby number, $\mathrm{Ro} \equiv V/(fL)$, which is the ratio of the neglected advection and tendency terms to the Coriolis terms in the momentum equation, is an indicator of the validity of this geostrophic approximation (f is the Coriolis parameter and V is a characteristic wind speed). When

Ro << 1, advection terms may be neglected and the geostrophic approximation is useful; for Ro ~ 1, the approximation is not valid. For a wind speed $V \sim 20$ m s^{-1} and $f \sim 10^{-4}$s^{-1}, the Rossby number will be 0.2, which is of order one, when the length scale $L \sim 100$ km. Figure 30.2 shows this to be in the range of meso-β phenomena. (2) When moist convection is an important feature of the initial conditions, it may be necessary to include latent heating effects in the initialization.

In summary, methods such as normal model initialization and procedures using geostrophic balance may have value for large meso-α circulations. However, satisfactory techniques have yet to be developed that permit initialization of meso-β and small meso-α phenomena, particularly those in which latent heating and gravity wave effects are important.

30.3. The Concept of a Nested Grid

The nested-grid concept is fundamental to all the mesoscale models discussed here. Because of the finite size and speed of computers, numerical models are capable of resolving phenomena over only a limited range of horizontal scales. For example, regional-scale numerical models, which also are referred to as meso-α-scale or subsynoptic-scale models, use a horizontal grid spacing on the order of 50–200 km, so as to be capable of resolving phenomena with scales of several hundred kilometers in the small-scale end of the meso-α range (Fig. 30.2). Since the domain of such models would typically extend over at least several thousand kilometers, it is reasonable to expect that such models would be capable of simulating a variety of phenomena, ranging in size from the domain size (> 2000 km) down to 3–4 times the grid spacing (~ 200 km).

In fact, if the computer resources were available, one could create a mesoscale model spanning the Northern Hemisphere with a 50 km resolution. Such a model would be capable of resolving all scales from $L > 10{,}000$ km (planetary waves) down to $L \sim 200$ km (small meso-α phenomena such as mesoscale convective systems). However, it is not cost effective to use a 50 km resolution over Europe and Asia if one is interested only in forecasting or simulating mesoscale features over North America. The planetary and synoptic-scale waves over the Eastern Hemisphere would certainly be important to a medium-range forecast (2–5 days) of North America, but these waves ($L > 2000$ km) could be very well resolved by a grid size of 200 km or more.

Hence, a reasonable strategy would be to use a grid that varies in the horizontal from a fine mesh over the mesoscale area to a coarser mesh over the rest of the globe. Ideally, one could use a mesh that varied smoothly from 50 km in the primary region of interest, North America in this case, to 200 km in the regions far from this zone. Another procedure, which is more convenient, is to define a zone of constant grid resolution that is located or "nested" within a coarser mesh outer domain.

The ability of a finite-difference model to represent a propagating disturbance depends on the local grid size (particularly when the scale of the disturbance is 4–6 times the grid size). Therefore, the effect of the interface

between fine and coarse grids upon a disturbance propagating through it will be larger or smaller as the ratio between the inner and outer grid sizes is chosen to be larger or smaller. To reduce this interface effect, one could use a telescoping nested grid, in which each successively coarser grid has a mesh size that is double the size of the next interior mesh.

Phillips (1979) used this basic approach in the Nested-Grid Model (NGM) that is the regional forecasting model in NMC's new Regional Analysis and Forecasting System. The NGM consists of three grids, denoted A, B, and C (Fig. 30.3), as defined on a polar stereographic projection of the Northern Hemisphere.

The grid-nesting approach used in the NGM involves a so-called two-way interaction. This terminology is used because information is communicated not only down-scale from the larger grids A and B to smallest grid C, for example, but also up-scale from grid C to grids B and A. That is, not only will changes in synoptic-scale features in region A be sensed by grid points in region C, but also mesoscale disturbances within region C will influence the larger scale solution in region A.

Most mesoscale models in use today, other than those simulating hurricanes, use only one-way interaction. In this simpler nesting procedure, the nested model receives information from the larger domain model in which it is nested; however, it is unable to influence the outer solution. In fact, the large-domain solution need not be integrated with the one-way nested solution but rather may be run by itself at an earlier time. The previous NMC operational forecasting system with the LFM and global PE models was an example of one-way interaction (Fig. 30.4). After the global PE model was run, its predicted fields were used to provide lateral boundary conditions for the nested LFM model forecast during the next forecast cycle.

Although one-way interaction produces a physical approximation that causes some errors in the numerical solution (Phillips and Shukla, 1973), it also provides certain conveniences to the modeler. The nested mesoscale model can be run repeatedly using different numerical and physical parameters but with the larger-scale host model only run once. The forecast from the host model (e.g., the LFM or spectral PE forecast) is needed so that time-varying lateral boundary conditions can be constructed that are used by the nested simulation. In fact, researchers frequently use observations alone, taken over the time period of the simulation, to prescribe these lateral boundary fields. Note that, in the latter case, the model is no longer a predictive system, since it then requires knowledge about the observed fields along the model boundaries after the initial time.

30.4. Examples of Mesoscale Simulations and Forecasts

Several examples of mesoscale simulations/forecasts will serve to indicate the philosophy behind the design and use of two types of models: (1) regional-scale (meso-α) models treating a springtime severe storm outbreak and (2) nested hurricane models. In the latter case, two different types of simulations/forecasts are presented: (a) simulated changes in the structure of an idealized storm during landfall and (b) examples of storm-track

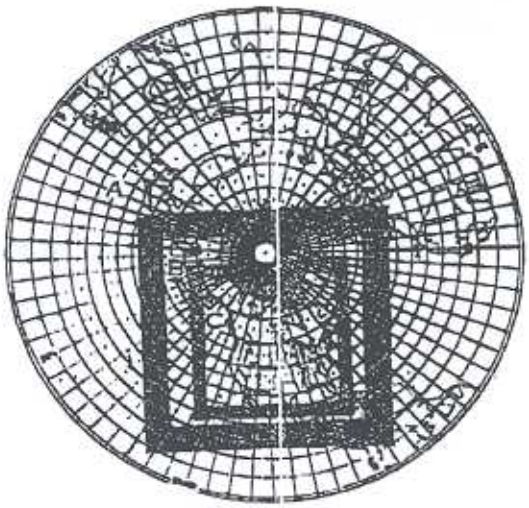

Figure 30.3. The three-grid configuration of the Nested Grid Model (NGM), an example of two-way interaction. The outer grid A is hemispheric. Grids B and C have two and four times, respectively, the resolution of Grid A. The shaded areas indicate zones where adjacent grids overlap. (After Hoke, 1984.)

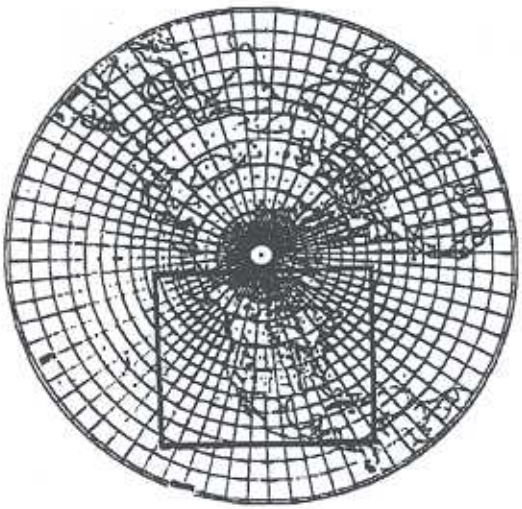

Figure 30.4. Forecast domain (indicated by heavy line) of the Limited-area Fine-Mesh (LFM) model, an example of a one-way interacting model. Boundary conditions for the LFM model are derived from the global spectral model forecast made during the previous prediction cycle. (After Hoke, 1984.)

forecasts. (Simulations of two other classes of mesoscale phenomena, namely terrain-forced circulations and isolated convective storms, are described in Ch. 22 and Ch. 15 respectively.)

All the models treated here use the hydrostatic approximation (i.e., the vertical momentum equation reduces to a balance between buoyancy and vertical pressure gradient forces; advection and tendency terms are neglected). Most have a primary meso-α-scale outer domain (with resolved horizontal scales ~200–2000 km), although several solutions resolve meso-β scales (i.e., 20–200 km).

30.4.1. Comparison of Regional-Scale Models

Regional-scale numerical models, that is, models that resolve subsynoptic or meso-α-scale phenomena, should be capable of treating a variety of phenomena, ranging from synoptically forced phenomena, such as fronts and frontal circulations, to terrain-induced processes, such as mountain waves and land/sea-breeze effects. Ideally, such models should be able to represent warm-season mesoscale convective systems as well as wintertime snowstorms. For a regional-scale model to simulate all these diverse phenomena properly would seem to require complex and general portrayals of the different physical processes, such as subgrid-scale convection and turbulence, surface energy balance, and radiation, suited to each flow regime and phenomenon to be modeled. However, Anthes *et al.* (1982) demonstrated that a model with

rather simple physics can produce realistic simulations of a variety of different mesoscale processes in the same solution. Similarly, Orlanski and Polinsky (1984) produced good simulations of both winter- and springtime precipitation events, using a model with simplified physical processes. However, although such successes are evident in the research literature, one should expect that different models, using different initialization procedures and data and different lateral boundary information, will produce significantly different results. This point is emphasized in the examples that follow.

The LFM model was one of the earliest regional-scale numerical models; its resolution of roughly 160 km in middle latitudes permits it to resolve meso-α phenomena with horizontal scales ~600 km. Operational use of the LFM model has been shown to produce a significant improvement in forecasting skill over North America (Shuman, 1978). However, although predictions of surface temperature and 500 mb winds have improved, accuracy of precipitation forecasts, particularly those indicating locations where rainfall should exceed 1 inch in a 24 h period, has remained relatively unchanged.

Analysis of seasonal variations in the success of LFM rainfall predictions shows that forecast skill is best for winter and worst for summer (Fawcett, 1977). This trend is explainable by the fact that wintertime precipitation is stable and is forced on scales that are meso-α or larger; on the other hand, rainfall during the warm season is often convective, the most unstable scales occurring in the range of meso-γ or small meso-β. Thus, while the winter precipitation scales are largely resolvable by a regional-scale model, the most unstable summertime scales are not and may need to be parameterized. In the latter case, one would hope that the convective system as a whole, which is made up of individual convective elements, is organized by resolvable dynamical processes, such as frontal lifting. If it is not, as in the case of summertime isolated thunderstorms, then the resulting convection will not be predictable, in a deterministic sense, by regional-scale models.

Although a numerical forecast may predict the unstable environment properly, the forecast model may still not be able to produce observed severe weather or precipitation in a given case. In such a case, the failure of the model to produce convective activity at a given location may be due to its inability to resolve the triggering mechanism that initiated the convection. As discussed in Sec. 30.2., any numerical prediction uses incomplete mesoscale initial conditions and approximate subgrid-scale parameterizations to forecast mesoscale phenomena of interest. Hence, once cannot expect a model to provide a deterministic forecast of mesoscale precipitation events when the triggering event, such as a propagating gravity wave or some other meso-β or meso-γ disturbance, is not resolvable by the model or, if it is resolvable, is not represented properly by the initial and/or boundary conditions. This point needs to be emphasized in any discussion of numerical prediction of mesoscale precipitation.

It is instructive to compare precipitation forecasts produced by several different mesoscale models for a single case, the first observing day of SESAME-AVE (Severe Environmental Storms and Mesoscale Experiment–Atmospheric Variability Experiment). For the period of this case (1200

Table 30.1. Characteristics of simulations and forecasts of the first observing day of SESAME-AVE

	Model	Integration period (GMTh/day)	Convective parameterization	Initial condition data source
I	LFM-II [NMC Operational]	(a) 12/10–12/11 (b) 12/9–12/11	Convective Adjustment	NMC observed
II	Anthes *et al.* (1982) Benjamin & Carlson (1986) [NCAR-PSU]	12/10–12/11	Kuo-type (Anthes)	NMC observed
III	Kaplan *et al.* (1982) [MASS]	12/10–12/11	Resolved	NMC observed
IV	Mills & Hayden (1983) [ANMRC]	(a) 12/10–03/11 (b) 21/10–03/11	Kuo-type	(a) NMC observed (b) Satellite obs.
V	Orlanski *et al.* (1983) [GFDL/HIBU]	12/9–12/11	Convective Adjustment	(a) NMC observed (b) FGGE observed
VI	Orlanski & Polinsky (1984) [GFDL/MAC]	12/9–12/11	Resolved	NMC observed
VII	Kalb (1984) [Drexel/LAMPS]	21/10–06/11	Plume-cloud type (Kreitzberg-Perkey)	SESAME observed
VIII	Kuo & Anthes (1984) [NCAR-PSU]	12/10–12/11	Kuo-type (Anthes)	SESAME observed
IX	Chang *et al.* (1984) [Drexel/LAMPS]	12/10–12/11	Plume-cloud type (Kreitzberg-Perkey)	NMC observed
X	Ross (1983) [GFDL/BES]	12/10-12/11	Resolved	SESAME observed

GMT, 10 April–1200 GMT, 11 April 1979), at least eight different models have been run to produce ten different simulations/forecasts. Table 30.1 summarizes the salient characteristics of each simulation/forecast.

Grid and Domain Sizes

The models may be roughly divided into two groups according to grid size: (1) those in the range of 67–160 km, models I, II, IV, V, VI, and IX, and (2) those in the range of 20–50 km, models III, VII, VIII, and X. Using the criterion that a model resolves phenomena with horizontal scales greater than or equal to roughly four times the horizontal grid size, one could categorize the former group as meso-α models. On the other hand, models in the latter group are resolving some meso-β-scale phenomena (i.e., scales less

Table 30.1. Continued

Model	Lateral boundary data source	Horizontal grid size [middle-latitude] (km)*	Domain array size	No. of vertical levels
I	NMC hemispheric PE forecast	110	79×67	7
II	NMC observed	111	37×37	11
III	NMC observed	41	157×117	14
IV	NMC observed	67	101×71	10
V	GFDL global spectral PE forecast	156	49×27	9
VI	NMC observed	160	21×21	17
		60	51×51	
VII	SESAME observed (21, 0C, and 12GMT only)	35	44×50	15
VIII	SESAME observed	50	45×34	11
IX	NMC observed	140	41×35	15
X	SESAME observed	40 20	21×21 41×41	17

* Cases II, IV, V, VI, VIII, and X use models with staggered grid meshes, i.e., grid configurations in which not all variables are at the same spatial location. For these models, the grid size shown here, which is the distance between the nearest like-variable points, is an overestimation of the actual effective grid size when compared with the other, unstaggered-grid models in this table.

than 200 km). Regarding domain size, the models in the former group all cover at least two-thirds of the United States. In the latter group, the large domain size of case III allows it to cover most of North America, whereas cases VII and VIII include only the south-central United States and case X covers only part of Oklahoma and Texas. All models except the LFM-II (model I) contain at least nine vertical levels.

Integration Periods

The integration periods of six of the ten cases extend over the 24 h SESAME-I period, 1200 GMT, 10 April, to 1200 GMT, 11 April. The two meso-α GFDL simulations, V and VI, have 48 h periods from 1200 GMT, 9 April, to 1200 GMT, 11 April, as does one of the LFM solutions. Cases IV and VII are integrated for only a portion of the 24 h period.

Parameterization Schemes

Several different parameterization schemes are employed (Table 30.1). Models I and V use a convective-adjustment-type scheme (see, e.g., Miyakoda, 1973). Solutions II and VIII use a Kuo-type parameterization (Anthes, 1977). Case IV also uses a Kuo scheme for one solution but typically involves solutions without convective parameterization. The model used in cases VII and IX employs a parameterization based on a plume-type cloud model (Kreitzberg and Perkey, 1976). Finally, three of the solutions, III, VI, and X, do not specifically parameterize convection but rather include only resolved moist convection.

Data Sources

Four different data sources are used for initial (and lateral boundary) conditions. (The detailed procedures by which the observed data are converted to the model grids may differ considerably among the cases and may have a significant effect on the resulting simulations. See general discussion of the procedures in Chs. 8, 24, 26, this volume. However, such details are beyond the limits of the present discussion.) The designation NMC indicates the standard operational data set used by the National Meteorological Center to initialize its forecast models. Because these are operational data, the data set is restricted to include only those upper-air reports that met the cut-off time for reporting. Solutions I, II, III, IV, Va, VI, and IX use these data. In several of these cases, significant as well as mandatory levels are used from the soundings. Solution II also uses subjective enhancement to emphasize mesoscale features. The second data set, designated FGGE, is used only in solution Vb. These data were collected as part of the 1979 First GARP Global Experiment (FGGE) and were prepared at the Geophysical Fluid Dynamics Laboratory (GFDL) through a dynamic assimilation method (Ploshay *et al.*, 1983). The data encompass the upper-air reports included in the NMC operational analysis as well as late reports not meeting the operational cut-off time and special observations from normally data-sparse regions over the ocean. The third data set, designated SESAME, was obtained from the SESAME field experiment and was employed in solutions VII, VIII, and X. The upper-air data used in these experiments were obtained from a rawinsonde network over the central United States with average spacing of roughly 250 km and with soundings made every 3 h from 1200 GMT 10 April, to 1200 GMT, 11 April (Alberty *et al.*, 1979). Note that solution VII uses reports only at 2100, 0000, and 1200 GMT, whereas solutions VIII and X use all sounding times. Finally, in case IVb, high-resolution satellite sounding

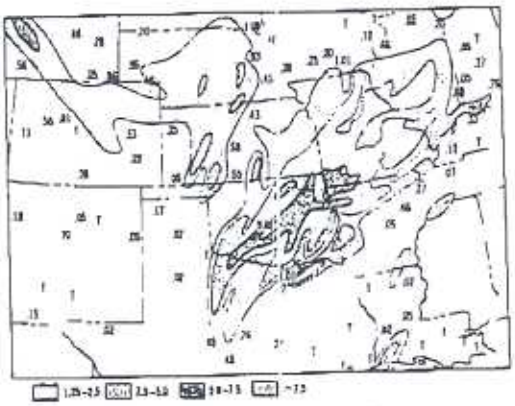

Figure 30.5. Analysis of observed 24 h accumulated precipitation for the period 1200 GMT, 10 April, to 1200 GMT, 11 April 1979. Maximum (9.40 cm) occurred over central Oklahoma. Contours are in centimeters. (Analysis courtesy of the Heavy Precipitation Forecasting Group of NMC.)

data from two orbital passes (2140 and 2200 GMT) over the United States are used to enhance temperature and moisture fields in the model solution at 2100 GMT, 10 April.

Synoptic Conditions

The synoptic conditions associated with the 10–11 April case have been described by several authors (e.g., Moore and Fuelberg, 1981) and are discussed only briefly here as they relate to the discussion that follows. At 1200 GMT, 10 April, a deepening surface low was located over Colorado. A surface cold front extended south into eastern New Mexico, and a warm front ran east-west along the gulf coast. Warm moist air was being advected northward from the Gulf of Mexico beneath a capping inversion over eastern Texas. The warm front moved northward during the period, reaching the Texas-Oklahoma border about 0000 GMT, 11 April, while the cold front slowly moved into western Texas.

Two separate convective systems can be identified to have occurred during the period. The first developed about 1800 GMT, 10 April, to the west and south of the Red River Valley, which forms the Texas-Oklahoma border. The southernmost part of this system then moved east, producing numerous tornadoes and hail storms (see Alberty *et al.*, 1979). A second system began over west-central Texas about 0130 GMT, 11 April, and developed into a slow-moving squall line that extended to the northeast and persisted for the next 9 hours. The combined effect of these two systems was to produce the 24 h accumulation of precipitation shown in Fig. 30.5, the heaviest rainfall having occurred over central Oklahoma about 0300 GMT, 11 April. Of particular note in Fig. 30.5 is the orientation of rainfall fields in a streaked pattern from southwest to northeast over Texas, Oklahoma, and Missouri. This alignment reflects the orientation of the 11 April squall line, which was determined by the strong middle- and upper-level winds over the region. This pattern will be shown to differ quite dramatically from most of the model rainfall patterns which show more of an east-west alignment.

30.4.2. Comparison of Results in Modeled Precipitation

The model precipitation results have been taken from the work of several different groups and therefore tend to differ with regard to the period of accumulation (as well as the contour interval used for each display). The reader should note that the maps of "observed" rainfall differ considerably from each other. This reflects the well-known fact that precipitation patterns, particularly in convective situations like this, have spatial and temporal scales that make them difficult, if not impossible, to analyze in a coherent and objective way from relatively sparse rain-gauge network data (see e.g., Krietzberg, 1979; Wilson and Brandes, 1979). (The Heavy Precipitation Forecasting Group at NMC produced Fig. 30.5 through the use of satellite cloud photography and radar summaries in addition to rain-gauge reports.) Accordingly, the comparison made here can only be qualitative with regard to differences between the simulations and "reality."

Also note that the results of case IV are not discussed here, because Mills and Hayden (1983) did not present explicit precipitation results, except to indicate regions of vertical motion over Oklahoma that might produce precipitation in their model.

Case I

Two LFM precipitation forecasts (case I of Table 30.1) are shown in Fig. 30.6 for the same 24 h period as that in Fig. 30.5. No results from a global PE model are given here; however, relative to the discussion of Sec. 30.2, the LFM results provide some indication of what such a PE prediction might be like. Figure 30.6a shows the accumulated rainfall from the LFM-II forecast, initialized at 1200 GMT, 10 April, most of the rainfall having occurred during the last 12 hours. Figure 30.6b shows the 24–48 h accumulation from the LFM forecast initialized at 1200 GMT, 9 April. The 0–24 h forecast (Fig. 30.6a) provides a reasonable forecast of rainfall amounts

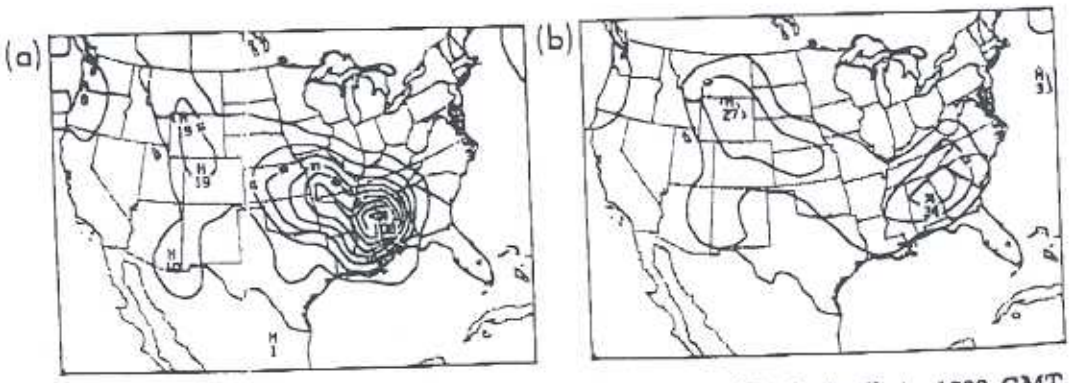

Figure 30.6. Precipitation amounts for the period 1200 GMT, 10 April, to 1200 GMT, 11 April, as predicted by two LFM–II forecasts: (a) 0–24 h forecast, initialized 1200 GMT, 10 April, and (b) 24–48 h forecast, initialized 1200 GMT, 9 April. Labeled contours are in millimeters; the outermost contour is 2.5 mm. H indicates local maximum; X indicates figure maximum. (Data courtesy of NMC.)

over Oklahoma, Texas, and Missouri, but predicts a maximum of 10.8 cm over Alabama and Mississippi where no rainfall occurred. A maximum in the southeast also was forecast in the 24–48 h result, which showed precipitation less than 1 cm in Oklahoma and Missouri. In addition, both model results suggest a southeast-to-northwest alignment of the rainfall distribution, in contrast to the southwest-to-northeast pattern of the observations.

Case II

Figure 30.7b shows the 24 h accumulated precipitation from solution II by Anthes *et al.* (1982), which uses the NCAR-PSU mesoscale model (Anthes and Warner, 1978) with enhanced NMC observed data for initial and boundary conditions (started at 1200 GMT, 10 April). The analyzed precipitation map, Fig. 30.7a (with logarithmic contouring scale), shows agreement with Fig. 30.5 with regard to pattern over the eastern portion of the heavy rainfall area, although more significant differences are evident to the west. Model results indicate precipitation >1.48 cm (level 5 of their scale) in a region on the east side of the domain oriented approximately west to east. Comparable rainfall was observed in this region over Oklahoma and Missouri but not to the east and occurred in a swath running southwest to northeast. (There is a suggestion of the squall line in the level-3 and -4 contours of the model results over Texas as there was in Fig. 30.7a.) The large rainfall

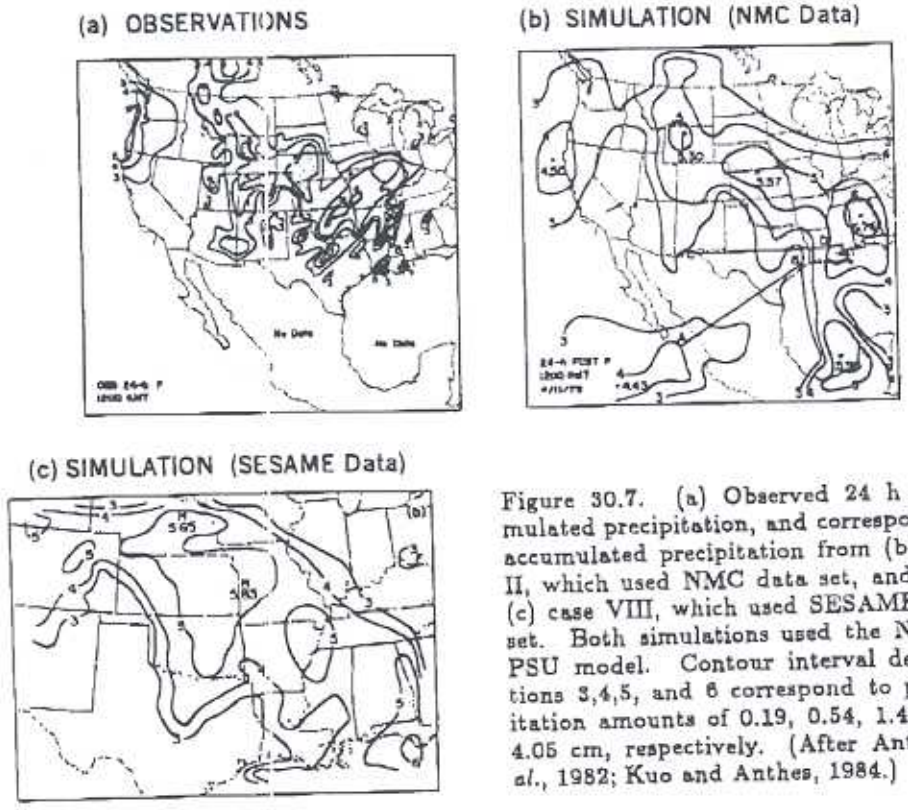

Figure 30.7. (a) Observed 24 h accumulated precipitation, and corresponding accumulated precipitation from (b) case II, which used NMC data set, and from (c) case VIII, which used SESAME data set. Both simulations used the NCAR-PSU model. Contour interval designations 3,4,5, and 6 correspond to precipitation amounts of 0.19, 0.54, 1.48, and 4.05 cm, respectively. (After Anthes *et al.*, 1982; Kuo and Anthes, 1984.)

maximum over Mississippi was hypothesized by Anthes *et al.* (1982) and later demonstrated by Benjamin (1983) to be caused by erroneous low-level convergence in the initial conditions along the gulf coast, which was believed to be due to differing data densities from land to sea. (Figure 30.7c shows results from Case VIII, discussed below.)

Case III

Solutions for case III are shown in Fig. 30.8. Kaplan *et al.* (1982) used their MASS mesoscale model to produce this 24 h simulation using NMC observed data for initial conditions and apparently also for lateral boundary conditions. The analysis of observed rainfall amounts for each 12 h period used only rain gauge data from first-order NWS stations and therefore contains considerably less detail than the analyses in Figs. 30.5 and 30.7. The model results, which were produced by resolvable moist convection only (more recent versions of the MASS model use a convective parameterization scheme), show small precipitation amounts during the first 12 h of the solution. This result reflects the tendency of numerical models to under-predict precipitation during the early stages of an integration as well as the bias of resolvable convection in a mesoscale model to respond more slowly than parameterized convection (because of the model's reliance on resolved vertical motion to advect moisture aloft and the requirement for the entire grid box to reach saturation before convection can occur). The model precipitation during the next 12 h, when the major precipitation occurred, shows heaviest amounts over Missouri, but relatively weaker amounts over Okla-

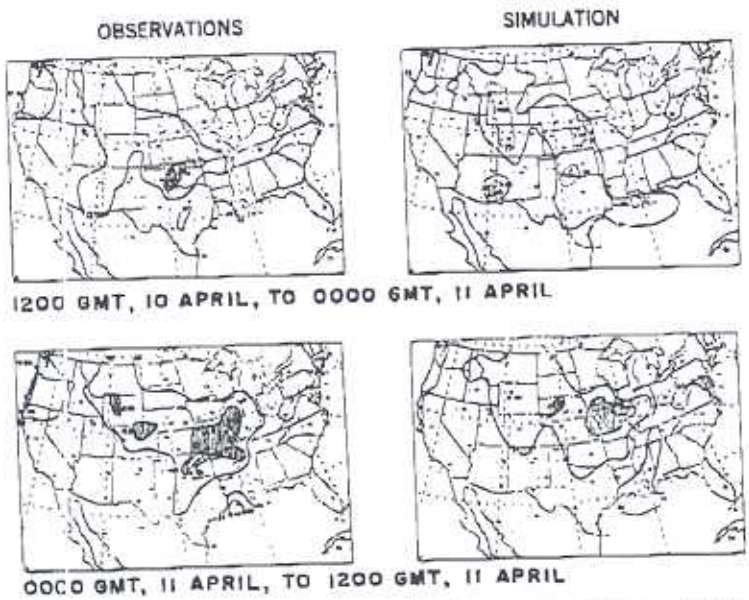

Figure 30.8. Observed accumulated precipitation (first-order NWS rainfall measurements only) and results from MASS model (Solution III) for successive 12 h periods. Contour intervals: 0.25,12.5,25.0,37.5 mm. (After Kaplan *et al.*, 1982.)

homa where the heaviest precipitation was observed to occur. No significant rainfall occurs in the southeast, in agreement with observations.

Case V

Figure 30.9 shows the 24 h amounts for 1200 GMT, 10 April, to 1200 GMT, 11 April, from forecast solutions Va and Vb reported by Orlanski *et al.* (1983). As with the LFM model, these are true forecasts rather than simulations; they were obtained from the limited-area GFDL/HIBU (Hydrometeorological Institute and Belgrade University [Yugoslavia]) model (see, e.g., Mesinger and Strickler, 1982) nested within the GFDL global spectral model (Gordon and Stern, 1982). Both the spectral and limited-area models were initialized at 1200 GMT, 9 April. In the first run, solution Va, the NMC operational analysis was used for initialization of the HIBU and spectral models; in the second, solution Vb, the special FGGE data set, analyzed by GFDL. was employed. Both solutions were run to 48 h. The precipitation forecasts for the last 24 h of both runs show great similarity to each other and to the LFM result over the southeast United States. Again, this result does not appear in the observed rainfall, obtained by a hand analysis of the primary NWS station data.

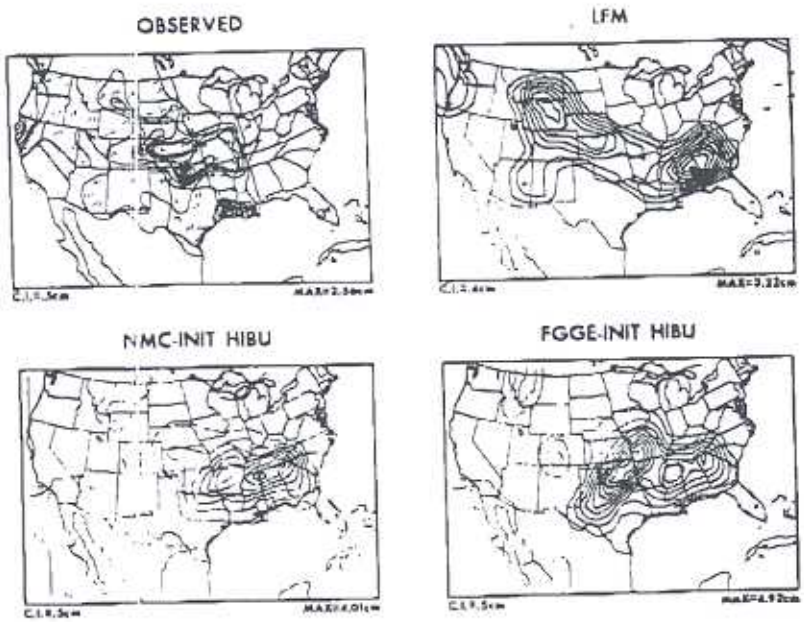

Figure 30.9. Accumulated precipitation for period from 1200 GMT, 10 April, to 1200 GMT, 11 April: as observed (from first-order NWS stations); according to LFM-II prediction (Cases 1), started 1200 GMT, 9 April; as forecast by GFDL/HIBU model using NMC initial conditions (Solution Va); and as forecast by GFDL/HIBU model using GFDL–FGGE initial conditions (Solution Vb). Contour interval and maximum are shown below each frame. (After Orlanski *et al.*, 1983.)

Figure 30.10. Accumulated precipitation (1200 GMT, 10 April, to 1200 GMT, 11 April) from GFDL/MAC model (Solution VI). Contours are in centimeters. (Figure courtesy of Orlanski and Shaginaw.)

Orlanski *et al.* (1983) attributed this erroneous precipitation in the southeast to the model's over-intensification of the warm front that moved north from the Gulf of Mexico. The modeled rainfall occurred along and ahead of this front. Orlanski's suggestion may also be the physical explanation of why Benjamin (1983) was able to eliminate this precipitation by changing his treatment of data along the Gulf Coast. In fact, when he started his run—1200 GMT, 10 April—the warm front was positioned along the coast line. Therefore, by reducing the data contrast, presumably of both wind and temperature, across the coast line, he was effectively reducing the initial intensity of the warm front.

The new and unique feature of these results, compared with earlier model results, is the large precipitation band in solution Vb running from southwest to northeast over Texas, Oklahoma, and Missouri (Fig. 30.9c). This is the first strong indication of the squall line character apparent in Fig. 30.5. The unique feature of this solution is the use of the FGGE data set, which includes improved observations over the data-sparse Pacific Ocean. The effect of this seems to have been to increase the upper-level winds over this region, thereby intensifying the surface cold front and its associated cross-stream circulation. This apparently provided the lifting for the convection and probably also increased the low-level transport of moist air from the Gulf that fueled the convective system. (In fact, whereas previous solutions tended to underestimate the effect of the cold front, this solution tends to overestimate it.)

Case VI

The 24 h precipitation pattern from solution VI was produced by Orlanski and Shaginaw (see Orlanski and Polinsky, 1984) using the GFDL/MAC model (Ross and Orlanski, 1982) with initial and boundary conditions derived from the NMC analysis. The western portion of the major precipitation zone (Fig. 30.10) has the same location as the observed pattern (as does the

local rainfall maximum over Kansas), but the modeled pattern extends more to the east. The anomalous precipitation to the east has been reduced considerably in this solution, compared, for example, with the LFM solution (Fig. 30.6a), suggesting that the influence of the warm front has been reduced. However, the major region of rainfall still occurs too far to the east; also, the absence of a southwest-to-northeast pattern indicates that the cold frontal intensity over Oklahoma and Texas remains too weak.

Case VII

Solution VII, performed by Kalb (1984, 1985) using the Drexel/LAMPS (Limited Area Mesoscale Prediction System) model (Perkey, 1976), is different from the previous solutions in several ways. First, the model was initialized at the asynoptic time, 2100 GMT, 10 April, using only SESAME data for the initial conditions and for the boundary conditions at 0000 and 1200 GMT of 11 April. In addition, only mandatory-level, observed geopotential height data were used in a nonlinear balance equation to determine the wind field above 1250 m (the nondivergent part of the observed winds was used below 1250 m). This was done in order to simulate a procedure of using satellite temperature soundings to produce the initial mass and momentum fields for the model.

A major effect of the choice of the initialization procedure and starting time was to produce several short waves in the simulation. One of these waves persisted and moved northward over Oklahoma and Kansas during the 9 h simulation. Figure 30.11 shows a composite of 700 mb geopotential heights and precipitation rates from the solution at 0300 GMT, 11 April, and the observed radar summary at 0235 GMT. Although no accumulated precipitation is shown, the two precipitation rates, both resolved and parameterized (convective), indicate the effect of the short wave and are supported to some extent by the radar summary. The squall line shown in the radar summary is also suggested by a tongue of increased relative humidity (see Kalb, 1985) but is not evident in the rainfall rates.

Cases VIII, IX, and X

Case VIII involves another simulation that uses the NCAR-PSU model. However, this solution uses a smaller domain (primarily encompassing the coverage of the regional-scale SESAME network) with a grid resolution of 50 km, rather than the 111 km used in case II. In addition, both the initial and boundary data used in the simulation were obtained from the 3 h SESAME rawinsonde observations. Figure 30.7c shows the accumulated precipitation from this solution. The broad zone of weaker rainfall (levels 3 and 4) still shows the same orientation as in case II. However, the regions of heavier rainfall (level 5, >1.48 cm) now have a north-south orientation over Oklahoma and Missouri. This result is also found in case X, which also used the SESAME data set.

Case X (Fig. 30.12) was performed by Ross (1983) using the GFDL/BES model (similar to the GFDL/MAC model) on an 800 × 800 km domain over

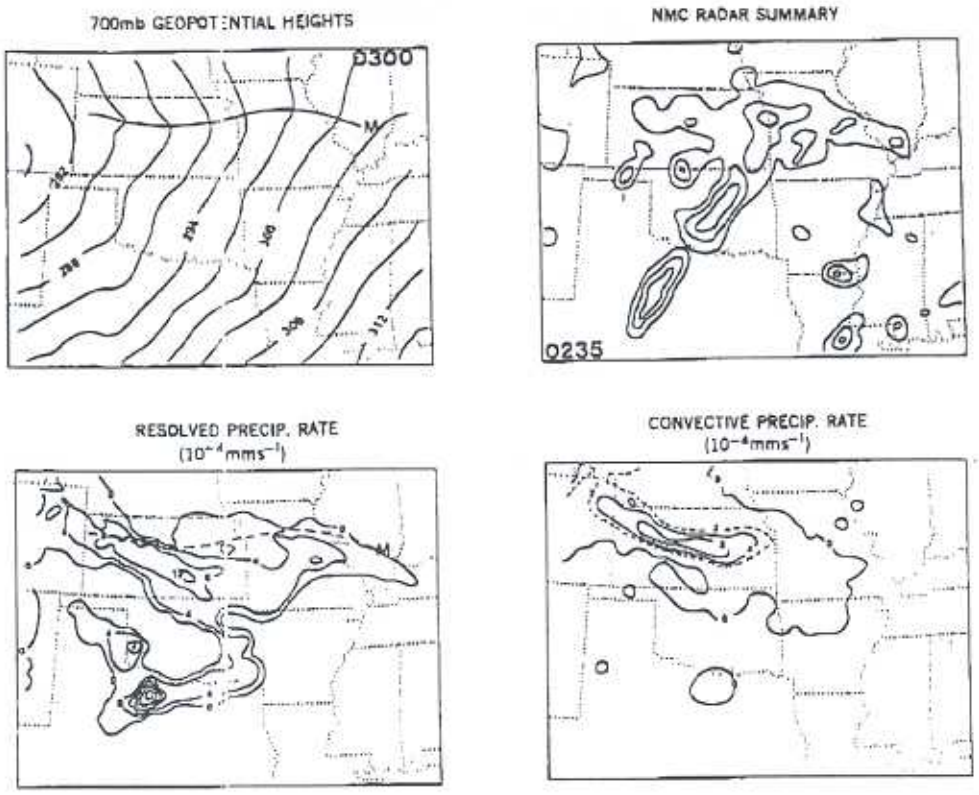

Figure 30.11. Geopotential heights at 700 mb for 0300 GMT, 11 April, of Solution VII (contours are in tens of meters); NMC radar summary at 0235 GMT; precipitation rate resolved by model at 0300 GMT; convected precipitation rate parameterized by model at same time. (After Kalb, 1985.)

southern Oklahoma and northeastern Texas. The precipitation accumulated at 3 h intervals is compared with observations at several different times during the 24 h integration. Simulations with 40 km and 20 km grid size are compared with observations. The observations were objectively analyzed from hourly rain-gauge data and reflect the great spatial variability of the rainfall data. The squall line structure is clearly evident for the period 0300–0600 GMT, 11 April, although the simulation provides a more continuous rainfall areal coverage than the rather sparse observations do. Ross found that the use of SESAME winds and the associated temperature field, and proximity of the boundary conditions to the location of the squall line were both necessary to represent the cold front system properly and thereby to produce a realistic squall line structure in the simulation. This supports the conclusions made earlier with regard to solutions Va and Vb: the enhanced FGGE data set produced the proper orientation of the heavy precipitation zone over Oklahoma whereas the operational (NMC) data set did not. Also this agrees with the improved precipitation results from case VIII (Fig. 30.7c), which used the SESAME data, compared with results from case II (Fig. 30.7b),

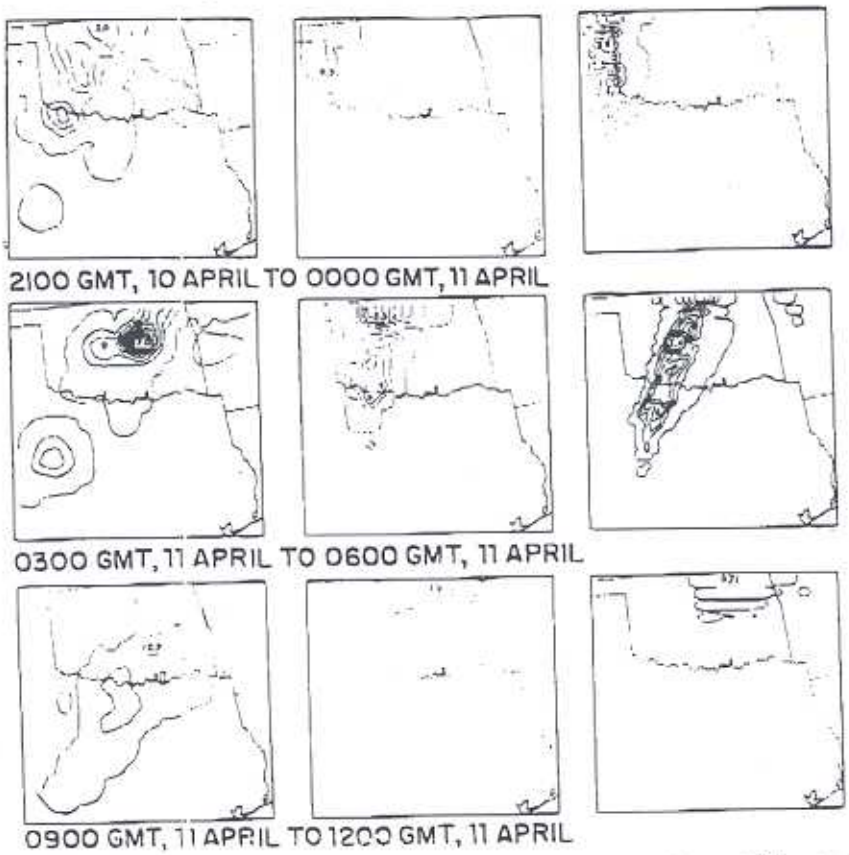

Figure 30.12. Comparison of 3 h accumulated precipitation at three different times: as observed (left column), as modeled for Case X with 40 km grid size (center column); and from the same model with 20 km grid size (right column). Contour intervals are 0.5 cm. (After Ross, 1983.)

which used NMC data. (The greater proximity of the upstream boundary in the former case probably also played a role in this improved simulation.) Although the correct mass and momentum fields were shown to be important in defining the forcing for the squall line in case X, the relative humidity field was found to control the structure and intensity of the resulting squall line.

The apparent sensitivity of rainfall results to the initial (and boundary) momentum fields agrees with the findings of the meso-α simulations in case IX as described by Chang *et al.* (1984). Using the Drexel/LAMPS model employed in case VII, but with a 140 km grid size, Chang *et al.* performed two simulations of the 24 h SESAME period that were identical except for the wind fields used to initialize the model. By altering the first-guess wind field in their initialization for 1200 GMT, 10 April, primarily by excluding a single wind observation over northwestern Mexico, they produced a considerable intensification in the jet streak over California and Mexico in the model's initial conditions. Compared with the solution based on a complete initial wind data set, the solution with the overly intense jet produced heav-

ier precipitation over Oklahoma and enhanced the unverified rainfall over the southeastern states (the latter result being similar to what was found in many of the other solutions reviewed above). The authors concluded that the prediction of the severe storm environment can be very sensitive to uncertainties in the initial wind field used for the forecast.

Conclusions From Precipitation Results

There is some difficulty in comparing modeled precipitation patterns with observations, partly because of the difficulty in producing a representative picture of the actual precipitation amounts that occurred. One would expect some differences between modeled and observed rainfall results, because of the considerable model variation in grid size, model physics, etc. Certainly, actual accumulated rainfall magnitudes differ widely as do details of rainfall patterns. However, although there are significant differences between model formulations, several features are common to many of them, namely, the erroneous rainfall in the southeast and the absence of an intense squall line over the south-central United States. These similarities suggest the possibility of similar biases in many of the different mesoscale models as well as a possible strong dependence of model solutions upon potentially inadequate initial and lateral boundary conditions. Work is still needed to identify these biases and the sensitivity of model precipitation and associated forcing mechanisms to different initial, boundary, and surface data.

30.4.3. Hurricane Modeling

Tropical cyclones are ideal candidates for nested-mesh models because they are compact and most of the smaller scale convective features and large gradients are near the vortex center. Because of this characteristic structure of hurricanes, several research groups have developed three-dimensional mesoscale models that use telescoping nested-grid systems, in which the finest mesh is near the center and meshes grow progressively coarser outward from the center (Mathur, 1974; Ley and Elsberry, 1976; Jones, 1977; Ookochi, 1978; Kurihara *et al.*, 1979). Most of these models also have the capability of shifting the interior grids relative to coarser outer grids so as to maintain the high-resolution mesh over the hurricane center as the storm moves. As an example, the telescoping nested-grid model, used by the Hurricane Group at GFDL (Kurihara *et al.*, 1979; Kurihara and Bender, 1980) is described here in detail.

GFDL's Nested-Grid Hurricane Model

In this triply nested model, the grid is defined on constant latitude and longitude lines. The three meshes, A, B, and C, are progressively finer—1, 1/3, and 1/6 degree, respectively—and have corresponding domain sizes (Fig. 30.13). The outermost lateral boundaries (for mesh A) are either open (i.e., use conditions from an externally defined state through one-way interaction) or cyclic (i.e., disturbances passing out through the boundary on one side will enter the domain on the opposite side). Each internal boundary

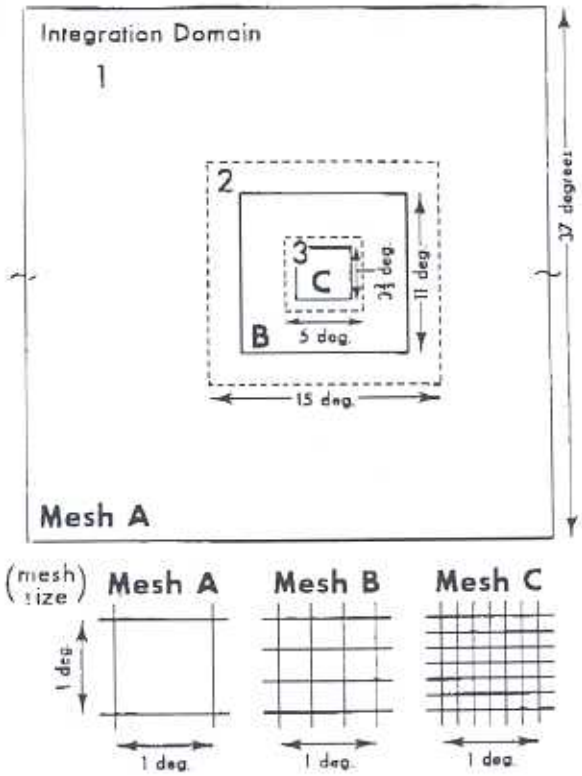

Figure 30.13. Horizontal structure of the triply-nested-mesh system, showing (above) domain and (below) grid sizes (not same scale as domain sizes). (After Kurihara and Bender, 1980.)

between mesh domains has an interface zone (between the dashed and solid lines in the figure), several coarse grid elements wide, in which the two-way interaction takes place during the time-marching of the model. The fluxes of physical quantities such as momentum and moisture through the interface are conserved by this procedure.

The movable meshes B and C are positioned with respect to the center of gravity of the surface pressure depression. For example, when this center moves in mesh C by more than the grid size Δ_B of the next coarser mesh (B), the fine mesh C is moved by the distance Δ_B in the direction of movement so as to recenter the storm. This movement is accomplished by converting coarse to fine grid points at the leading edge and replacing fine with coarse points at the trailing edge. Mesh B is moved relative to A in a similar manner, as recentering becomes necessary. As one might expect, computational noise is generated during this procedure. This noise is suppressed in the GFDL model through the use of a time-integration method that selectively damps high-frequency noise, and by nonlinear horizontal viscosity and occasional spatial smoothing.

Comparison of propagating vortex solutions with and without the nesting procedure demonstrates several advantages of nesting. First, as shown in the landfall simulation (next section), the detailed structure of the hurricane, including the wind field, surface pressure, and precipitation patterns, is represented much more satisfactorily in the nested model. In addition, the motion of the storm as a whole is altered significantly when the movable-nested-mesh system is used (Kurihara and Bender, 1980). This improvement seems to be due to the improved numerical as well as physical representation of the storm. Although such advantages are clearly desirable in a research mode, they must be weighted against the considerable increase in computational expense that would be incurred if a high-resolution nested model were used operationally.

Simulation of Landfall

The landfall of a hurricane is discussed in Ch. 14. The simulation of an idealized landfall event by the GFDL hurricane model is described here as an example of hurricane modeling in a research mode. Issues concerning initialization of the model for a real-data case and complications due to contrasting air masses, topography, etc., are not addressed in this study but are obviously important for an operational forecast. Other research simulations of landfall have been done by Moss and Jones (1978), Tuleya and Kurihara (1978), and Chang (1982).

GFDL's simulation (Tuleya *et al.*, 1984) deals with a simplified landfall situation. However, the capability of the simulation to be rerun with different conditions, such as reduced land surface temperature or varying land surface roughness, permits evaluation of the importance of each effect. In the solution presented here, the land surface is characterized as having the same moisture availability as the ocean surface, but a reduced surface temperature of 298 K (ocean value = 302 K) and an increased surface roughness length z_o of 25 cm. (The ocean value is typically less than 1 cm.) The large-scale wind field in the simulation consists of an approximately constant easterly wind of 10 m s^{-1}.

The hurricane is initialized in the model by adding an appropriate non-divergent vortex wind field to the basic background conditions. At the beginning of the simulation, ocean surface conditions are used over the entire domain; also, cyclic east-west boundaries are applied during an initial adjustment period. After the model has been integrated for 55 h of model time, the cyclic conditions on eastern and western boundaries are replaced by open boundaries; also, land surface conditions are imposed at all latitudes west of a longitude that is 8° west of the storm center. Landfall then occurs at 76.3 h.

As the cyclone encounters the change in surface conditions, the sudden increase in surface roughness, with its associated increase in drag, produces a drop in the low-level wind speed and a larger inflow angle of parcel trajectories into the hurricane. (These features were observed in Hurricane Frederic by Powell, 1982.) Figure 30.14 shows the evolution of the wind field in the lowest level above the surface as the storm encounters land. At 73 h, which

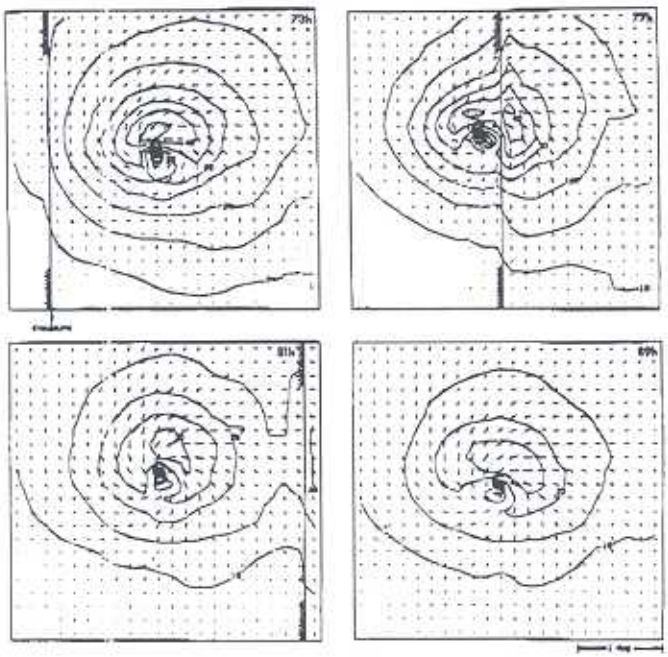

Figure 30.14. Analysis of winds at the first level above the surface within the mesh C domain of the landfall experiment at 73, 77, 81, and 89 h. The storm center defined by the surface pressure is indicated by a heavy dot. Contours indicate wind speed (m s^{-1}). Vectors show wind direction and magnitude. Land is to the west (left) of the indicated coastline. (After Tuleya *et al.*, 1984.)

is prior to landfall, the wind maximum is to the right and somewhat forward of the storm center (surface pressure minimum). Just after landfall (77 h), several wind peaks are evident. In fact, the location of the peak wind speed oscillates after this time but tends to occur, on average, at a right-rear position relative to the storm center. Winds decrease below hurricane force (which is defined as >33 m s^{-1}) by 81 h (hurricane force winds penetrate 165 km inland) and continue to drop thereafter. However, comparison of the hurricane motion with a control run that includes only ocean surface conditions shows only minor deflection (~50 km at 90 h) of the storm track due to landfall.

Figure 30.15 shows an analysis of rainfall rates and surface isobars for the times represented in Fig. 30.14. Because of the increased convergence within the storm, caused by the sudden change in surface drag, average precipitation rates increase slightly at landfall. Subsequently the area of heavy precipitation (>2.9 cm h^{-1}) begins to decrease 2 h later. The rainfall rates and areal coverage are similar to those estimated over land by Parrish *et al.* (1982) for Hurricane Frederic. However, their observation of a 50% increase in the area of convection at landfall is larger than that shown in the present simulations, probably because of differences in land surface conditions.

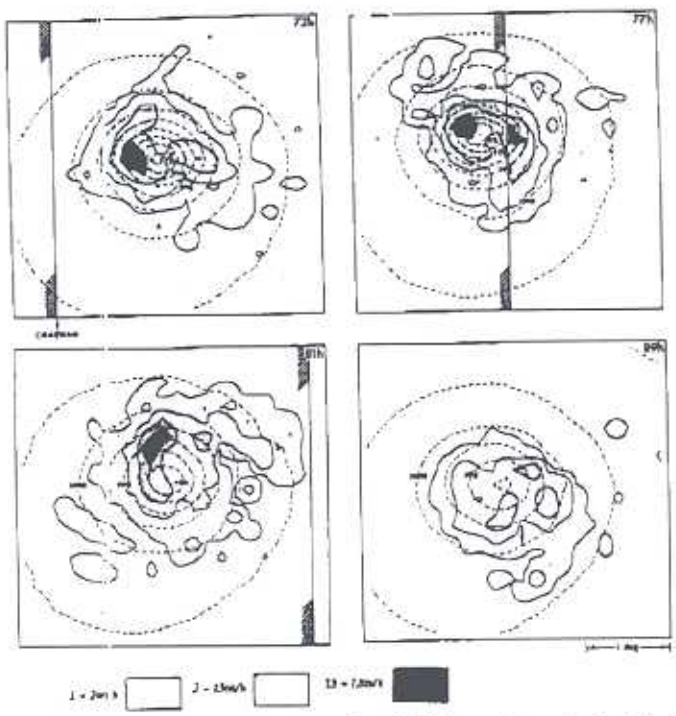

Figure 30.15. Analysis of rainfall rates for the landfall experiment, for the domain and times represented in Fig. 30.14. Dashed lines show isobars of surface pressure in 5 mb intervals. (After Tuleya *et al.*, 1984.)

The realistic simulation of the landfall event can be attributed to the 4° decrease in the land surface temperature as well as the increased surface roughness. The decay, indicated by the rise in surface pressure in Fig. 30.15, is due to the associated reduction in surface evaporation. Although the availability of surface moisture was the same over land as over ocean, the cooler land temperature decreased the surface evaporation rate, thereby reducing the water vapor available to the storm. In addition, the cool land conditions caused a decrease in the conditional instability of the storm environment and an alteration of the planetary boundary layer. Hence, the energy source that maintains the storm, the latent heating due to this convective instability, is reduced and the storm decays as it moves inland.

Recent experiments (Bender *et al.*, 1985) have shown that topographical influences may enhance the decay rate through their disorganizing effect on the storm system. Topography also intensifies the precipitation rate at landfall and affects the storm track.

An Operational Hurricane Forecast Model

The above description of a hurricane simulation indicates what may be possible operationally in the future. However, current operational modeling does not attempt to predict intensity or to resolve detailed features of the

hurricane, such as winds and precipitation patterns. The primary and vitally important objective of present-day operational models is the prediction of storm movement. Storm track forecast models are operational in three different organizations: the National Meteorological Center (Hovermale and Livezey, 1977); the U.S. Navy's Joint Typhoon Warning Center (Harrison and Fiorino, 1982); and the Japan Meteorological Agency (Ookochi, 1978). Following is a description of how NMC produces a storm track forecast, using its Movable Fine-Mesh (MFM) model.

The MFM model is a limited-area model designed for on-call use, to resolve severe mesoscale weather phenomena such as hurricanes and other heavy-precipitation weather systems. A typical configuration for the model consists of 10 vertical levels, a horizontal domain of 3000 × 3000 km, and 60 km grid spacing. The model uses fields from the NMC global spectral (or hemispheric grid-point) forecast to provide lateral boundary conditions in a one-way interaction mode. Also, in order to keep the hurricane away from the lateral boundaries, the mesh moves (relative to the global model) in a manner similar to that described for the GFDL model.

Given the limited computer resources available at NMC prior to 1983 and the typical paucity of detailed mesoscale observations of hurricanes in an operational time frame, NMC initialized the MFM model with a hurricane vortex derived from an idealized conceptual model rather than from observations. (The 60 km resolution of the model is unable to resolve the detailed inner core of the hurricane, anyway.)

The procedure used in 1975–76 to initialize the model was as follows:

- The standard NMC global analysis is interpolated to the MFM model; any small-scale features due to the presence of the hurricane are filtered out. This establishes the basic steering flow in the initial conditions.
- A two-dimensional (2-D), axisymmetric hurricane model, similar in its physics to the 3-D MFM model, is run using a representative tropical sounding and warm ocean until a quasi-steady hurricane is produced (1–2 minutes of IBM 360/195 time). This storm is in balance with respect to the 2-D model and the MFM model physics. However, it does not contain asymmetric features such as large-scale vertical wind shear and beta effects, i.e., effects due to changes in the Coriolis parameter across the storm. The latter may be included to some extent by modifying the 2-D wind field through a gradient wind relation.
- The resulting mass and momentum fields are then added, as perturbations, to the smoothed steering flow provided in step 1, and the 3-D MFM model is then run for the 48 h period of the forecast (using boundary conditions provided by the NMC global forecast).

As one might expect, the merging of the modeled vortex from step 2 with the background steering flow of step 1 produces an adjustment period during the early stages of the MFM forecast. Certain characteristics of the initial storm, such as its intensity and asymmetric features, affect the subsequent storm-track prediction. Figure 30.16 shows an example of the influence of these initial-condition features on track forecasts of Hurricane Eloise. The

first forecast, made operationally in 1975, included an overly strong and symmetric initial vortex. The resulting model vortex (solid line) moved too rapidly northward, compared with observations (indicated by the hurricane symbols in Fig. 30.16) and was not pushed eastward by a propagating middle-latitude trough passing through the region until it was only several hundred kilometers from landfall. In a later experimental forecast, the intensity of the initial vortex was reduced, and the wind field was corrected somewhat for β-effect asymmetries. These changes caused the model hurricane to move northward more slowly (dashed line). As a result, the trough encountered the storm more to the south, thereby pushing it farther to the east and producing a very accurate prediction of landfall location. (However, the predicted landfall time seems to be too late.)

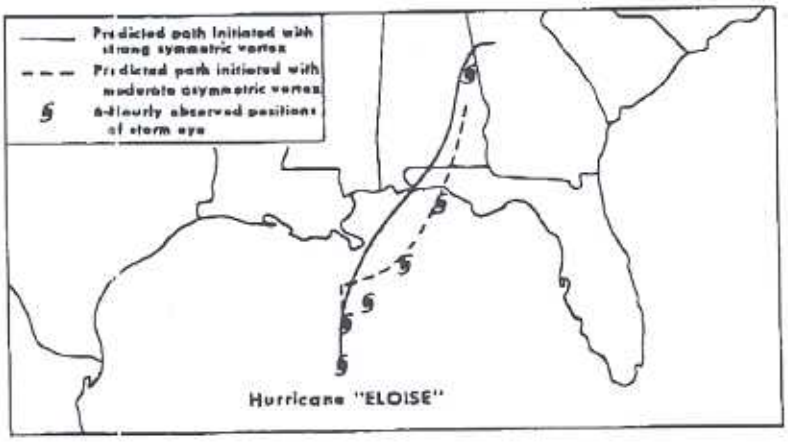

Figure 30.16. Observed track of Hurricane Eloise compared with two predicted tracks based on two different initial vortex conditions. (From a figure provided by John Hovermale.)

This example indicates how some of the many factors involved in a hurricane forecast can alter the storm-track prediction. Some of these factors can be controlled through improvements in the initialization procedure and enhancements of the dynamical model, such as increasing grid resolution. For example, a more recent version of the operational MFM model uses a three-dimensionally derived vortex to reduce initial adjustment effects in the forecast and thereby to improve short-range (0–24 h) predictions. Finally, a good forecast of the synoptic-scale conditions, used to prescribe lateral boundary conditions, is important in this case as in regional model predictions for forecast periods beyond a day or so.

REFERENCES

Alberty, R. L., D. W. Burgess, C. E. Hane, and J. F. Weaver, 1979: SESAME 1979 operations summary. NOAA Environmental Research Laboratories, Boulder, Colo., 253 pp.

Anthes, R. A., 1977: A cumulus parameterization scheme utilising a one-dimensional cloud model. *Mon. Wea.*

Rev., 105, 270–286

Anthes, R. A., 1982: *Tropical Cyclones—Their Evolution, Structure and Effects.* Meteor. Monogr. 41, American Meteorological Society, Boston, Mass., 208 pp.

Anthes, R. A., 1983: Regional models of the atmosphere in middle latitudes. *Mon. Wea. Rev.*, 111, 1306–1335.

Anthes, R. A., and T. T. Warner, 1978: Development of hydrodynamic models suitable for air pollution and other mesometeorological studies. *Mon. Wea. Rev.*, 106, 1045–1078.

Anthes, R. A., Y.-H. Kuo, S. G. Benjamin, and Y.-F. Li, 1982: The evolution of the mesoscale environment of severe local storms: Preliminary modeling results. *Mon. Wea. Rev.*, 110, 1187–1213.

Arakawa, A., and W. H. Shubert, 1974: Interaction of a cumulus cloud ensemble with the large-scale environment, Part I. *J. Atmos. Sci.*, 31, 674–701.

Bender, M. A., R. E. Tuleya, and Y. Kurihara, 1985: A numerical study of the effect of a mountain range on a landfalling tropical cyclone. *Mon. Wea. Rev.*, 113, 567–582.

Benjamin, S. G., 1983: Some effects of surface heating and topography on the regional severe storm environment. Ph.D. dissertation, The Pennsylvania State University, College Park, Pa., 265 pp.

Benjamin, S. G., and T. N. Carlson, 1986: Some effects of surface heating and topography on the regional severe storm environment. Part I: Three-dimensional simulations. *Mon. Wea. Rev.*, 114, 307–329.

Carlson, T. N., S. G. Benjamin, G. S. Forbes, and Y.-F. Li, 1983: Elevated mixed layers in the regional severe storm environment: Conceptual model and case studies. *Mon. Wea. Rev.*, 111, 1453–1473.

Chang, C. B., D. J. Perkey, and C. W. Kreitzberg, 1984: Impact of initial wind field on the forecast of a severe storm environment. Proceedings, 10th Conference on Weather Forecasting and Analysis, 1984, Clearwater Beach, Fla., American Meteorological Society, Boston, Mass., 513–520.

Chang, S. W., 1982: The orographic effects induced by an island mountain range on propagating tropical cyclones. *Mon. Wea. Rev.*, 110, 1255–1270.

Charney, J. G., 1954: Numerical prediction of cyclogenesis, *Proc. Natl. Acad. Sci.*, 40, 99–110.

Charney, J. G., R. Fjortoft, and J. von Neumann, 1950: Numerical integration of the barotropic vorticity equation. *Tellus*, 2, 237–254.

Clark, T. L., 1982: Cloud modeling in three spatial dimensions. *Hailstorms of the Central High Plains*, Vol. 1, National Hail Research Experiment, C.A. Knight and P. Squires (Eds.), Colorado Associated University Press, Boulder, 225–247.

Cotton, W. R., 1975: Theoretical cumulus dynamics. *Rev. Geophys. Space Phys.*, 13, 419–448.

Cressman, G. P., 1958: Barotropic divergence and very long atmospheric waves. *Mon. Wea. Rev.*, 86, 293–297.

Farley, R. D., and H. D. Orville, 1982: Cloud modeling in two spatial dimensions. *Hailstorms of the Central High Plains*, Vol. 1, National Hail Research Experiment, C.A. Knight and P. Squires (Eds.), Colorado Associated University Press, Boulder, 207–223.

Fawcett, E. B., 1977: Current capabilities in prediction at the National Weather Service's National Meteorological Center, *Bull. Amer. Meteor. Soc.*, 58, 143–149.

Gordon, C. T., and W. F. Stern, 1982: A description of the GFDL global spectral model, *Mon. Wea. Rev.*, 110, 625–644.

Haltiner, G. J., and R. T. Williams, 1980: *Numerical Prediction and Dynamic Meteorology.* 2nd ed., Wiley, New York, 477 pp.

Harrison, E. J., Jr., and M. Fiorino, 1982: A comprehensive test of the Navy Nested Tropical Cyclone Model. *Mon. Wea. Rev.*, 110, 645–650.

Hoke, J. E., 1984: Forecast results for NMC's new regional analysis and forecast system. Proceedings, 10th Conference on Weather Forecasting and Analysis, Clearwater Beach, Fla., American Meteorological Society, Boston, Mass., 418–423.

Hovermale, J. B., and R. E. Livezey, 1977: Three-year performance characteristics of the NMC hurricane model. Proceedings, 11th Technical Conference on Hurricanes and Tropical Meteorology, Mi-

ami, Fla., American Meteorological Society, Boston, Mass., 122–124.

Jones, R. W., 1977: A nested grid for a three-dimensional model of a tropical cyclone. *J. Atmos. Sci.*, **34**, 1528–1553.

Kalb, M. W., 1984: Initialization of a mesoscale model for April 10, 1979, using alternate data sources. NASA Contractor Report 3826, Marshall Space Flight Center, Ala., 230 pp.

Kalb, M. W., 1985: Results from a limited-area mesoscale numerical simulation for 10 April 1979. *Mon. Wea. Rev.*, **113**, 1644–1662.

Kaplan, M. L., J. W Zack, V. C. Wong, and J. J. Tuccillo, 1982: Initial results from a mesoscale atmospheric simulation system and comparison with the AVE-SESAME I data set. *Mon. Wea. Rev.*, **110**, 1564–1590.

Kreitzberg, C. W., 1979: Observing, analysing, and modeling mesoscale weather phenomena. *Rev. Geophys. Space Phys.*, **17**, 1852–1871.

Kreitzberg, C. W., and D. J. Perkey, 1976: Release of potential instability. Part I: A sequential plume model within a hydrostatic primitive equation model. *J. Atmos. Sci.*, **33**, 456–475.

Kuo, Y.-H., and R. A. Anthes, 1984: Accuracy of diagnostic heat and moisture budgets using SESAME-79 field data as revealed by observing system simulation experiments. *Mon. Wea. Rev.*, **112**, 1465–1481.

Kurihara, Y., and M. A. Bender, 1980: Use of a movable nested-mesh model for tracking a small vortex. *Mon. Wea. Rev.*, **108**, 1792–1809.

Kurihara, Y., G. J., Tripoli, and M. A. Bender, 1979: Design of a movable nested-mesh primitive equation model. *Mon. Wea. Rev.*, **107**, 239–249.

Ley, G. W., and R. L. Elsberry, 1976: Forecast of Typhoon Irma using a nested-grid model. *Mon. Wea. Rev.*, **104**, 1154–1161.

Mathur, M. B., 1974: A multiple-grid primitive equation model to simulate the development of an asymmetric hurricane (Isbell, 1964). *J. Atmos. Sci.*, **31**, 371–393.

Mesinger, F., and R. F. Strickler, 1982: Effect of mountains on Genoa cyclogenesis. *J. Meteor. Soc. Japan*, **60**, 326–338.

Mills, G. A., and C. M. Hayden, 1983: The use of high horizontal resolution satellite temperature and moisture profiles to initialize a mesoscale numerical weather prediction model—A severe weather event case study. *J. Climate Appl. Meteor.*, **22**, 649–663.

Miyakoda, K., 1973: Cumulative results of testing a meteorological-mathematical model: The description of the model. *Proc. Royal Irish Acad.*, **73**(A), 99–130.

Moore, J. T., and H. E. Fuelberg, 1981: A synoptic analysis of the first AVE-SESAME '79 period. *Bull. Amer. Meteor. Soc.*, **62**, 1577–1590.

Moss, M. S., and R. W. Jones, 1978: A numerical simulation of hurricane landfall. NOAA Tech. Memo. ERL NHEML-3, Environmental Research Laboratories, Boulder, Colo. (NTIS#PB-290 39817GA), 15 pp.

Ookochi, Y., 1978: Preliminary test of typhoon forecast with a moving multi-nested grid (MNG). *J. Meteor. Soc. Japan*, **56**, 571–583.

Ooyama, K. V., 1982: Conceptual evolution of the theory and modeling of the tropical cyclone. *J. Meteor. Soc. Japan*, **60**, 369–380.

Orlanski, I., 1975: A rational subdivision of scales for atmospheric processes. *Bull. Amer. Meteor. Soc.*, **56**, 527–530.

Orlanski, I., and L. Polinsky, 1984: Predictability of mesoscale phenomena. In Nowcasting II, Mesoscale Observations and Very Short-Range Forecasting (Proceedings, Second International Symposium on Nowcasting, 3–7 September 1984, Norrköping, Sweden), ESA SP-208, European Space Agency, Noordwijk, Netherlands, 271–280.

Orlanski, I., D. Miller, and K. Miyakoda, 1983: The impact of initialization analyses in the forecasting of precipitation patterns. WMO Workshop on Very Short-Range Forecasting Systems Research Aspects, Boulder, CO, 15–17 August 1983, Short- and Medium-Range Weather Prediction, Research Publication Series, No. 5, World Meteorological Organization, 59–62.

Parrish, J. R., R. W. Burpee, F. D. Marks, Jr., and R. Grebe, 1982: Rainfall patterns observed by digitized radar during the landfall of Hurricane Frederic (1979).

Mon. Wea. Rev., 110, 1933–1944.

Perkey, D. J., 1976: A description and preliminary results from a fine-mesh model for forecasting quantitative precipitation. *Mon. Wea. Rev.*, 104, 1513–1526.

Phillips, N. A., 1979: The nested grid model. NOAA Technical Report NWS 22, National Weather Service (NTIS#PB–299046/3GA), 80 pp.

Phillips, N. A., and J. Shukla, 1973: On the strategy of combining coarse and fine grid meshes in numerical weather prediction. *J. Appl. Meteor.*, 12, 763–770.

Pielke, R. A., 1981: Mesoscale numerical modeling. *Adv. Geophys.*, 23, 185–344.

Pielke, R. A., 1984: *Mesoscale Meteorological Modeling*. Academic Press, New York, 632 pp.

Platzman, G. W., 1979: The ENIAC computations of 1950—Gateway to numerical weather prediction. *Bull. Amer. Meteor. Soc.*, 60, 302–312.

Ploshay, J. J., R. K. White, and K. Miyakoda, 1983: FGGE level III-B daily global analyses, Part I (Dec. 1978–Feb. 1979). NOAA Data Report GFDL–1, Environmental Research Laboratories (NTIS#PB73–221051) 278 pp.

Powell, M. D., 1982: The transition of the Hurricane Frederic boundary wind field from the open Gulf of Mexico to landfall. *Mon. Wea. Rev.*, 110, 1912–1932.

Rosenthal, S. L., 1978: Numerical simulation of tropical cyclone development with latent heat released by the resolvable scales. I: Model description and preliminary results. *J. Atmos. Sci.*, 35, 258–271.

Ross, B. B., 1983: Sensitivity of meso-β scale precipitation forecasts to specification of initial and boundary data. Abstracts, 1st Conference on Mesoscale Meteorology, Norman, Okla., CIMMS, Univ. Oklahoma, Norman.

Ross, B. B., and I. Orlanski, 1978: The circulation associated with a cold front. Part II: moist case. *J. Atmos. Sci.*, 35, 445–465.

Ross, B. B., and I. Orlanski, 1982: The evolution of an observed cold front. Part I: Numerical simulation. *J. Atmos. Sci.*, 39, 296–327.

Schlesinger, R. E., 1982: Three-dimensional numerical modeling of convective storms: A review of milestones and challenges. Proceedings, 12th Conference on Severe Local Storms, San Antonio, Tex., American Meteorological Society, Boston, 506–515.

Shuman, F. G., 1978: Numerical weather prediction. *Bull. Amer. Meteor. Soc.*, 59, 5–17.

Shuman, F. G., and J. B. Hovermale, 1968: An operational six-layer primitive equation model. *J. Appl. Meteor.*, 7, 525–547.

Teweles, S., and H. Wobus, 1954: Verification of prognostic charts. *Bull. Amer. Meteor. Soc.*, 35, 455–463.

Tuleya, R. E., and Y. Kurihara, 1978: A numerical simulation of the landfall of tropical cyclones. *J. Atmos. Sci.*, 35, 242–257.

Tuleya, R. E., M. A. Bender, and Y. Kurihara, 1984: A simulation study of the landfall of tropical cyclones using a movable nested-mesh model. *Mon. Wea. Rev.*, 112, 124–136.

UCAR, 1983: The National STORM Program—Scientific and technological bases and major objectives. R. A. Anthes (Ed.), University Corporation for Atmospheric Research, Boulder, Colo., to NOAA, Contract NA81RAC00123, 520 pp.

Wilson, J. W., and E. A. Brandes, 1979: Radar measurements of rainfall summary. *Bull. Amer. Meteor. Soc.*, 60, 1048–1058.